Applied Physics Letters

RESEARCH ARTICLE | JANUARY 30 2024

Atomic layer self-transducing MoS_2 vibrating channel transistors with 0.5 pm/Hz$^{1/2}$ displacement sensitivity at room temperature

Special Collection: Critical Issues on the 2D-material-based field-effect transistors

S M Enamul Hoque Yousuf ; Philip X.-L. Feng

Appl. Phys. Lett. 124, 053503 (2024)
https://doi.org/10.1063/5.0170127

AIP Publishing

Applied Physics Letters ARTICLE pubs.aip.org/aip/apl

Atomic layer self-transducing MoS_2 vibrating channel transistors with 0.5 pm/Hz$^{1/2}$ displacement sensitivity at room temperature

Cite as: Appl. Phys. Lett. **124**, 053503 (2024); doi: 10.1063/5.0170127
Submitted: 1 August 2023 · Accepted: 3 January 2024 ·
Published Online: 30 January 2024

View Online Export Citation CrossMark

S M Enamul Hoque Yousuf and Philip X.-L. Feng[a)]

AFFILIATIONS

Electrical and Computer Engineering, Herbert Wertheim College of Engineering, University of Florida, Gainesville, Florida 32611, USA

Note: This paper is part of the APL Special Collection on Critical Issues on the 2D-material-based field-effect transistors.
[a)]**Author to whom correspondence should be addressed:** philip.feng@ufl.edu

ABSTRACT

We report on the experimental demonstration of high-performance suspended channel transistors with single- and bilayer (1L and 2L) molybdenum disulfide (MoS_2), and on operating them as vibrating channel transistors (VCTs) and exploiting their built-in dynamic electromechanical coupling to read out picoampere (pA) transconduction current directly at the vibrating tones, without frequency conversion or down-mixing, for picometer (pm)-scale motion detection at room temperature. The 1L- and 2L-MoS_2 VCTs exhibit excellent n-type transistor behavior with high mobility [150 cm^2/(V·s)] and small subthreshold swing (98 mV/dec). Their resonance motions are probed by directly measuring the small-signal drain-source currents (i_D). Electromechanical characteristics of the devices are extracted from the measured i_D, yielding resonances at $f_0 = 31.83$ MHz with quality factor $Q = 117$ and $f_0 = 21.43$ MHz with $Q = 110$ for 1L- and 2L-MoS_2 VCTs, respectively. The 2L-MoS_2 VCT demonstrates excellent current and displacement sensitivity ($S_i^{1/2} = 2$ pA/Hz$^{1/2}$ and $S_x^{1/2} = 0.5$ pm/Hz$^{1/2}$). We demonstrate f_0 tuning by controlling gate voltage V_G and achieve frequency tunability $\Delta f_0/f_0 \approx 8\%$ and resonance frequency change $\Delta f_0/\Delta V_G \approx 0.53$ kHz/mV. This study helps pave the way to realizing ultrasensitive self-transducing 2D nanoelectromechanical systems at room temperature, in all-electronic configurations, for on-chip applications.

Two-dimensional (2D) materials offer exquisite membranes with remarkable electrical, optical, and mechanical properties.[1] Integrating 2D membranes into resonant nanoelectromechanical systems (NEMS) enables new device platforms both for exploring fundamental physics and device applications.[2–5] Thanks to atomic-scale thickness, these 2D NEMS resonators can be highly responsive to external perturbations. The incorporation of 2D materials into NEMS resonators leads to electrically tunable devices with improved sensitivity and controllability by permitting the manipulation of resonant frequencies via the application of external electric fields.[6,7] Molybdenum disulfide (MoS_2), one of the most prominent members in the family of layered semiconductors in transition metal dichalcogenide (TMDCs), has been investigated recently in various device platforms, including transistors and NEMS resonators.[8–11] Monolayer and few-layer MoS_2 flakes are appealing candidates for electronic switching devices due to its high thermal stability up to 1100 °C,[12] surfaces free of dangling bonds, thickness-dependent bandgap ($E_g = 1.3$ eV for bulk and $E_g = 1.8$ eV for monolayer),[13] and enhanced room-temperature mobility up to 900 cm^2/(V·s).[14] Vibrating channel transistors (VCTs) employ suspended atomically thin 2D semiconducting crystals as channel materials, and the channels oscillate at the resonance modes of the VCTs in radio frequency (RF) bands.[15,16] VCTs can be incorporated into the back-end-of-line (BEOL) of complementary metal oxide semiconductor (CMOS) processors, enabling integrated frequency control elements with smaller footprints than oscillators demonstrated with discrete components.[17,18]

Electrical and optical excitation schemes can be used to excite the motions of the VCTs. To detect or probe the motions, different readout schemes have been explored including optical interferometry, capacitive sensing, and direct electrical readout. Optical interferometric readout scheme provides ultrasensitive displacement measurements to sub-pm/Hz$^{1/2}$ levels, while it requires laser and other precise but often off-chip components.[2] Ultracoherent optomechanical systems provide exceptional displacement sensitivity reaching 1.5 dB below the standard quantum limit (SQL) by exploiting strong quantum correlations.[19] However, to achieve such displacement sensitivity, the system requires cooling down to cryogenic temperature and does not permit room temperature operation. Toward all-electronic transduction, frequency modulation (FM) down-mixing scheme is generally utilized to

transduce the VCTs motions.[20–22] In addition to having to drive the device and sense its motion at different frequencies, extra electrical components, such as mixers, frequency synthesizers, and phase-locked loops, are often required to implement FM down-mixing, which increases circuit complexity and system expense. Phase noise of the local oscillator can introduce phase fluctuations in the down-mixed signal, thus limiting the sensitivity of the system. Ideally, without frequency downconversion, directly measuring the drain-source current (i_D) in a transistor configuration is the desirable straightforward approach to probing the resonance motion. Yet, this has been challenging due to large background signal coming from parasitic effects present in the circuit.[23] The oscillating current component induced by resonance motion is inherently small; thus, careful device design and calibration are necessary to resolve the resonance motion from direct i_D measurement without mixing or frequency conversion.

In this Letter, we report on all-electrical, ultrasensitive readout of the resonance motion of monolayer (1L) and bilayer (2L) MoS_2 VCTs by directly measuring i_D at the resonant motion frequencies. The 1L-MoS_2 device exhibits high on-current $I_{On} = 0.1\ \mu A/\mu m$, high on-off ratio $I_{On}/I_{Off} > 10^5$, excellent mobility $\mu_E = 150\ cm^2/(V{\cdot}s)$, and subthreshold swing $SS = 98$ mV/dec. Fitting i_D after subtracting background reveals resonance at $f_0 = 31.83$ MHz with $Q = 117$, current sensitivity $S_i^{1/2} = 7.2\ pA/Hz^{1/2}$, and displacement sensitivity $S_x^{1/2} = 2.9\ pm/Hz^{1/2}$. The 2L-$MoS_2$ device demonstrates $I_{On} = 0.07\ \mu A/\mu m$, $I_{On}/I_{Off} > 10^4$, $\mu_E = 79\ cm^2/(V{\cdot}s)$, $SS = 400$ mV/dec, $f_0 = 21.43$ MHz with $Q = 110$, $S_i^{1/2} = 2\ pA/Hz^{1/2}$, and $S_x^{1/2} = 0.5\ pm/Hz^{1/2}$. We demonstrate f_0 tuning by controlling gate voltage V_G and achieve fractional frequency tunability $\Delta f_0/f_0 \approx 8\%$ and resonance frequency change $\Delta f_0/\Delta V_G \approx 0.53$ kHz/mV by directly probing i_D. We also investigate the effect of drain voltage V_D on f_0 and Q of the 2L-MoS_2 VCT. Finally, we benchmark $S_x^{1/2}$ measured in this work with other detection schemes. These results hold promise for future ultrasensitive 2D NEMS integrated with CMOS.

The structure of a MoS_2 VCT on a SiO_2-on-sapphire substrate is illustrated in Fig. 1(a). The MoS_2 membrane is suspended over a 290 nm deep circular cavity with radius d and fully clamped on perimeter of the cavity, providing the drumhead resonator structure vibrating at its natural frequencies. Utilizing the Pt electrode located underneath, this configuration reduces the parasitic capacitance impact while providing local electrostatic gate control. For on-chip applications of VCTs, sapphire substrates allow patterning local gates to separately control multiple devices on the same chip. A variety of photolithography and etching techniques that are compatible with the state-of-the-art CMOS processes are used to fabricate the substrates (for a complete description of the fabrication process, see Sec. S1 in the supplementary material).[3] From a 2H semiconducting MoS_2 bulk crystal (purchased from 2D Semiconductors, SKU-BLK-MoS_2-SYN), we exfoliate the 2D MoS_2 flakes [Fig. 1(b)] using Scotch tape, pick them up with polydimethylsiloxane (PDMS), and transfer them on top of the prefabricated electrodes via all-dry transfer techniques. With this process, we fabricate VCTs in high-quality 1 and 2L MoS_2 flakes. We use Raman spectroscopy to determine the numbers of layers in the exfoliated flakes (see S2 in the supplementary material).

Applying a DC gate voltage V_G electrostatically attracts the membrane toward the local gate and stretches the membrane from its initial position to an equilibrium position z_0 [Fig. 1(c)]. Adding an RF voltage $v_g = v_{RF}\cos(\omega t)$ to V_G further induces small-signal mechanical vibration with amplitude δz from its initial equilibrium position z_0 due to varying electrostatic force [Fig. 1(d)]. The complex signal transduction pathways of converting the resonator motion into output voltage are shown in Fig. 1(e). The oscillating gate voltage v_g modifies electrical conductance of the channel by changing the carrier density $n = n_0 + \delta n$ in the suspended membrane. Applied oscillating voltage v_g also modulates the displacement $z = z_0 + \delta z$ of the membrane from its equilibrium position, inducing change in the gate-channel capacitance $C_{ch} = C_{ch0} + \delta C_{ch}$ and, thus, modifies the carrier concentration.

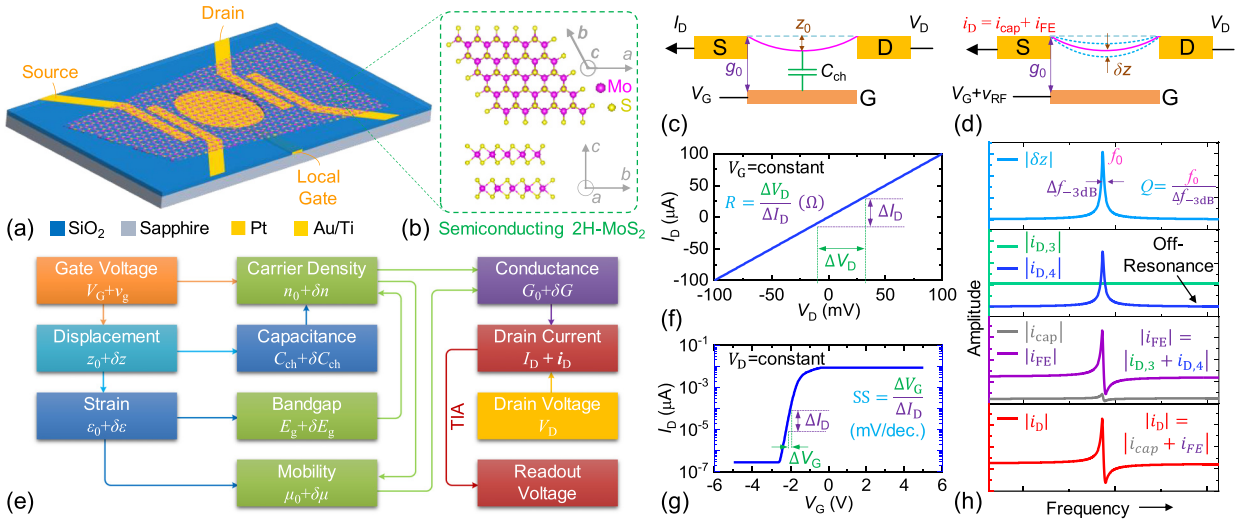

FIG. 1. (a) Schematic illustration of MoS_2 VCT consisting of single- or few-layer MoS_2 membranes. (b) Crystal structure of the semiconducting 2H-MoS_2 with orientation. Schematic of VCT under (c) DC and (d) RF gating. (e) Signal transduction diagram for transducing the motion of the MoS_2 VCT by directly reading out i_D. (f) Transport and (g) transfer characteristics of VCT under DC bias and gate voltages. (h) The magnitude of complex displacement amplitude (top panel) and different output current components (three lower panels) as a function of frequency.

The change in displacement also affects the strain $\varepsilon = \varepsilon_0 + \delta\varepsilon$ on the membrane, which, in turn, modifies the mobility of the charge carriers $\mu = \mu_0 + \delta\mu$ and bandgap of the material $E_g = E_{g0} + \delta E_g$. The electron mobility can be affected by changes in both n and ε. Therefore, the channel conductance $G = G_0 + \delta G$ is modulated by the components from both electrical and mechanical domains. By applying a small constant DC voltage V_D at the drain, an alternating current $I_D + i_D$ is drawn from the source electrode. A transimpedance amplifier (TIA) (FEMTO, Model: HCA-200M-20K-C) converts the current to voltage and is finally read out by a network analyzer (NA) (HP3577A).

Under only DC bias and gate voltages V_D and V_G, VCTs exhibit conventional transport and transfer characteristics. During transport measurement, V_D is swept, while V_G kept constant [Fig. 1(f)]. The total resistance including the contact resistance and channel resistance can be extracted from this measurement by taking the ratio $\Delta V_D/\Delta I_D$. The results also reveal the contact type between the semiconductor channel material and the metal electrodes either to be Ohmic or Schottky contact. Transfer characteristics, where V_G is swept, while V_D kept constant, reveal the switching behavior of the VCTs [Fig. 1(g)]. The subthreshold swing (SS), defined as the required V_G span for decade change in drain current during switching, measures abruptness of the transistor turn-on and the off-state leakage current. We can calculate the transconductance of the transistor as $g_m = dI_D/dV_G$ from the transfer curve. The motion of the MoS_2 VCT is driven electrostatically by applying v_g along with V_G to the gate. The vibrational displacement of the membrane from its equilibrium position can be written as[24]

$$\delta z = -\frac{dC_{ch}}{dz}\frac{V_G v_{RF}}{m_{eff}}\frac{1}{\omega_n^2 - \omega^2 + j\frac{\omega_n \omega}{Q}}, \quad (1)$$

where $C_{ch} = \epsilon A/g_0$ is the channel-gate capacitance, ϵ is the permittivity of the medium, $A = 0.25\pi d^2$ is the local gate-suspended channel coupling area, g_0 is the gap between the local gate and suspended membrane, m_{eff} and ω_n are effective mass and resonance frequency of the nth mode of the resonator, respectively, and ω is the frequency of the drive signal from the network analyzer. To directly readout the motion of the MoS_2 VCTs by probing i_D, we apply RF oscillating voltage $v_g = v_{RF}\sin(\omega t)$ to the gate electrode. The measured RF current has four components and can be expressed as

$$i_D = j\omega C_{tot} v_{RF} - \frac{j\omega C_{ch} V_G \delta z}{g_0} + g_m v_{RF} - \frac{g_m V_G \delta z}{g_0}. \quad (2)$$

Here, C_{tot} is the total capacitance of the device including the gate-membrane capacitance C_{ch} and parasitic capacitance $C_p = C_{GD} + C_{GS}$, and C_{GD} and C_{GS} being the gate–drain and gate–source capacitances, respectively. The first two terms in Eq. (2) originate from capacitive effects in the VCT, $i_{cap} = j\omega(C_{tot}v_{RF} - C_{ch}V_G\delta z/g_0) = i_{D,1} + i_{D,2}$, whereas the last two terms arise from field effect in the VCT, $i_{FE} = g_m(v_{RF} - V_G\delta z/g_0) = i_{D,3} + i_{D,4}$. The mechanical motion of the membrane contributes to the motional current $i_z = (-j\omega C_{ch} - g_m)V_G\delta z/g_0$. Figure 1(h) shows the different component of the output currents as a function of frequency (f) for a typical drumhead resonator. During f sweep, at f far away from the resonance frequency f_0, the current is dominated by the third term ($i_{D,3}$) of Eq. (2). When f moves toward f_0, the amplitude of vibration grows and starts to contribute to the field effect current i_{FE}. At f_0, the field effect current apexes due to maximum vibration amplitude of the VCT. At frequency slightly higher than f_0, the total field effect current drops due to opposite phase of $i_{D,3}$ and $i_{D,4}$. Far off resonance, the field effect current is again dominated by $i_{D,3}$. The total current (i_D) in the VCT is dominated by i_{FE} if the device design is optimized for small i_{cap}.

We first characterize the MoS_2 VCTs by measuring the transfer and transport characteristics using source measure units (SMUs) from a Keithley 4200A-SCS parameter analyzer and a custom-built probe station [Fig. 2(a)]. We apply V_G at the local gate to tension the membrane via electrostatic force. The equilibrium position of the membrane z_0 increases monotonically as we increase V_G [Fig. 2(b)]. Device 1 has a thickness of $h = 0.7$ nm, diameter of $d = 3\,\mu$m, Young's modulus of $E_Y = 270$ GPa,[25] Poisson's ratio of $\nu = 0.165$, mass density of $\rho = 5060\,\text{kg}\cdot\text{m}^{-3}$, effective mass of $m_{eff} = 6.75 \times 10^{-18}$ kg, initial strain of $\varepsilon = 0.0003$, channel length of $L = 6.9\,\mu$m, and a channel width of $w = 3\,\mu$m. Figure 2(c) depicts the measured transfer characteristics of device 1. The transistor demonstrates n-type behavior with high $I_{On} = 0.1$ μA/μm, I_{On}/I_{Off} exceeding 10^5, SS $\sim$ 98 mV/dec, $C_{ch} = 1.21$ fF (from COMSOL simulation), and $g_m = 13$ nS/μm, which yields field effect mobility $\mu_E = 150\,\text{cm}^2/(\text{V}\cdot\text{s})$. From transport characteristics of device 1 [Fig. 2(d)], the MoS_2/Au interface demonstrates Ohmic contact. Device 2 has $h = 1.4$ nm, $d = 3\,\mu$m, $E_Y = 200$ GPa,[25] $m_{eff} = 1.35 \times 10^{-17}$ kg, $\varepsilon = 0.0002$, $L = 6.9\,\mu$m, and $w = 3\,\mu$m. From the measured transfer characteristics of device 2 [Fig. 2(e)], this VCT demonstrates n-type behavior with $I_{On} = 0.07$ μA/μm, $I_{On}/I_{Off} > 10^4$, SS $\sim$ 400 mV/dec, $C_{ch} = 1.21$ fF, and $g_m = 7$ nS/μm, which yields field effect mobility $\mu_E = 79\,\text{cm}^2/(\text{V}\cdot\text{s})$.

Figure 3(a) shows the high-resolution optical image of device 1, indicating the 1L MoS_2 membrane on top of the microtrench. To detect the motion of the VCTs, we first excite the suspended MoS_2 membrane by applying RF voltage v_g from the network analyzer

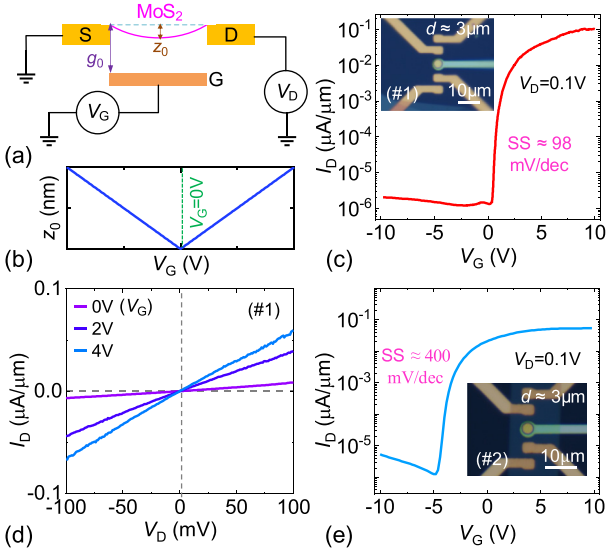

FIG. 2. (a) Illustration of DC characterization of MoS_2 VCTs. (b) Effect of V_G on maximum static deflection of MoS_2 membrane. (c) Transfer characteristics measured from the 1L MoS_2 VCT. Inset shows the optical image of this device. (d) Transport characteristics of 1L VCT showing Ohmic contact between 2D membrane and metal electrodes. (e) Measured I_D vs V_G of 2L MoS_2 VCT. Inset shows the optical image of the device.

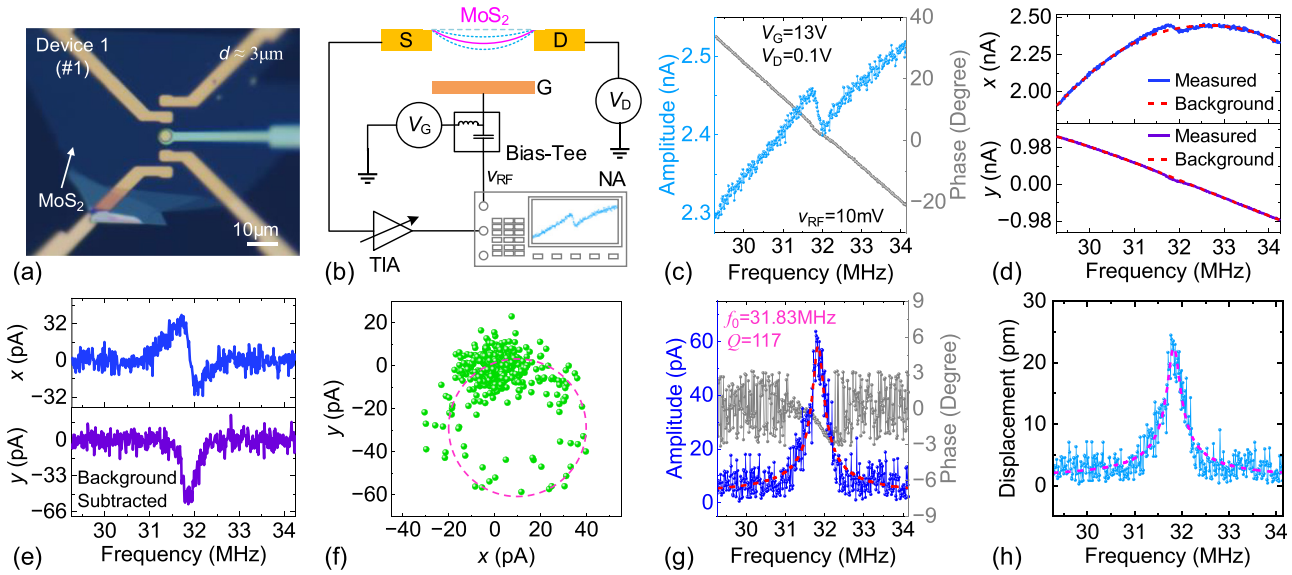

FIG. 3. (a) Optical image of VCT fabricated using 1L MoS_2 (device 1). Scale bar: 10 μm. (b) Resonance readout scheme for directly measuring the drain–source current of the VCT. NA: network analyzer, TIA: transimpedance amplifier. (c) Response of the VCT from direct i_D measurement. (d) Real (x) and imaginary (y) components of the measured signal. Fitted curves (dashed red lines) represent the background embedded with the signal. (e) Real (x) and imaginary (y) parts of the signal after background subtraction. (f) Trajectories in the rotating frame after subtracting the background. (g) Reconstructed current signal after subtracting the background signal showing clear resonance at $f_0 = 31.83$ MHz with $Q = 117$. (h) Extracted displacement of the membrane from the current amplitude.

combined with a DC voltage V_G using a bias tee to the local gate. A small DC voltage V_D is applied to the drain, and the source current is collected and passed through the TIA to convert the current to voltage. Finally, the voltage is measured and recorded using the network analyzer [Fig. 3(b)]. With $V_G = 13$ V, $V_D = 0.1$ V, and $v_{RF} = 10$ mV, we measure the response of the VCT, as shown in Fig. 3(c). The measured response shows a resonance peak embedded in a large background signal from parasitic capacitance. To decouple the resonance motion from the background, we separate the in-phase (x) and quadrature (y) components of the measured signal. We fit the background signal using higher order polynomial [Fig. 3(d)] using MATLAB and subtract the fitted background from the original signal. The background subtracted x and y components of the signal are shown in Fig. 3(e). Plotting the x and y components together reveals the dynamically stable points during driving the resonator over time. For the applied drive level, the system response clearly stays on a limit cycle [dashed red circle in Fig. 3(f)].

Finally, we reconstruct the current due to the resonance motion of the membrane by combining the x and y components [Fig. 3(g)]. The reconstructed signal shows a clear resonance at $f_0 = 31.83$ MHz with $Q = 117$. We are also able to see a clear shift of the phase at f_0. Using the motional current, we calculate the corresponding displacement by

$$\delta z = -\frac{i_z g_0}{V_G(g_m + jC_{ch}\omega)}. \quad (3)$$

We plot the magnitude of the displacement as a function of drive frequency [Fig. 3(h)] and resolve a maximum peak amplitude of 22 pm at f_0. The results show displacement sensitivity of 2.9 pm/Hz$^{1/2}$ with a standard deviation of 1.45 pm/Hz$^{1/2}$. The current sensitivity of device 1 is 7 pA/Hz$^{1/2}$ with a fluctuation of 3.7 pA/Hz$^{1/2}$.

Figure 4(a) shows the optical image of the 2L MoS_2 VCT with graphene contact. Graphene is used as a bridge between the semiconducting MoS_2 membrane and metal electrodes to reduce the contact resistance.[26] Lower contact resistance can lead to higher on-state current in the DC transfer and transport curves (such as in Fig. 2) of a VCT. The resonance signal of the VCT is mainly dominated by the device transconductance, channel vibration driven by the small-signal RF voltage, and parasitics [see Eq. (2)]. Effects of contact resistance on RF VCT's resonance response may warrant future experimental and theoretical studies. Raman signal with in-plane vibrational mode at $E_1^{2g} = 378.46\ cm^{-1}$ and out-of-plane vibrational mode at $A_{1g} = 400.41\ cm^{-1}$ with peak separation 21.95 cm^{-1} confirms the thickness of the MoS_2 flake.[27] By applying $V_G = 11$ V, $V_D = 0.1$ V, and $v_{RF} = 5$ mV, we record the response of the VCT, as shown in Fig. 4(b). To extract the motional current, we apply the same technique used in analyzing device 1 and remove the large background signal. Plotting the background-subtracted signal from device 2, we resolve f_0 at 21.43 MHz with $Q = 110$ [Fig. 4(c)]. The current sensitivity of device 2 is ~2 pA/Hz$^{1/2}$ with a fluctuation of ~1 pA/Hz$^{1/2}$. We extract the displacement of the vibrating membrane as a function of f using Eq. (3) and plot in Fig. 4(d). The displacement sensitivity of the device is 0.5 pm/Hz$^{1/2}$ with a fluctuation of 0.3 pm/Hz$^{1/2}$.

Next, we investigate the effect of varying V_G and demonstrate frequency tunability of the 2D NEMS resonator by directly measuring the drain–source current [Fig. 4(e)]. With $V_G < 7$ V, the signal is buried under the background signal. As we apply $V_G \geq 8$ V, the signal amplitude gradually increases. By fitting the background-subtracted signal, we calculate $f_0 = 19.85$ MHz at $V_G = 8$ V and $f_0 = 21.43$ MHz at $V_G = 11$ V [Fig. 4(f)]. Thus, the resonator shows fractional frequency tunability $\Delta f_0/f_0 \approx 8\%$ and resonance frequency change $\Delta f_0/\Delta V_G \approx 0.53$ kHz/mV. The Q decreases as we increase V_G due to the voltage loading effect. We study the effect of V_D on the response of the VCT

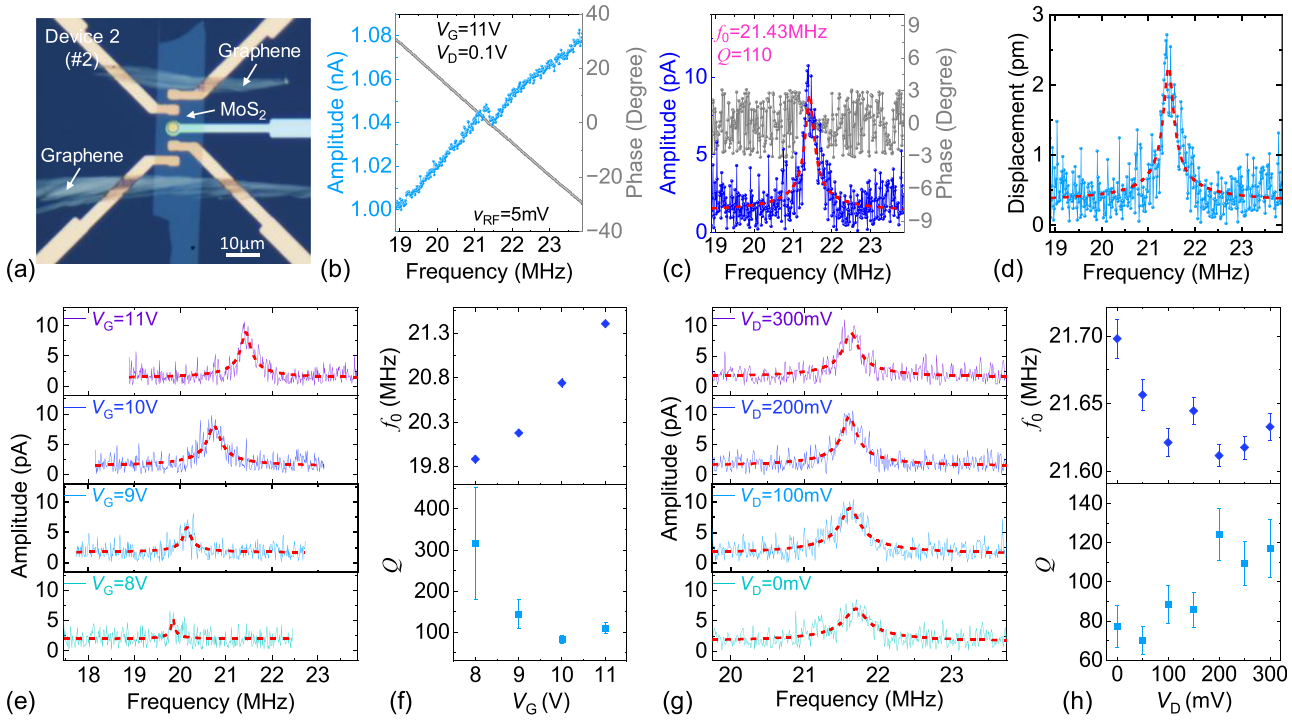

FIG. 4. (a) Optical image of VCT fabricated using 2L MoS_2 (device 2). Scale bar: 10 μm. (b) Response of the VCT from direct i_D measurement. (c) Signal after subtracting the background exhibiting $f_0 = 21.43$ MHz with $Q = 110$. (d) Extracted displacement of the vibrating membrane as a function of drive frequency. (e) Resonance frequency tuning by varying V_G and read out directly by measuring i_D. (f) Extracted f_0 (upper panel) and Q (lower panel) from (e). (g) Effect of bias voltage V_D on the response of the VCT. (h) Extracted f_0 (upper panel) and Q (lower panel) from (g).

by gradually increasing V_D from 0 to 300 mV [Fig. 4(g)]. As we increase V_D, the amplitude of the motional current increases. f_0 decreases slightly as we increase V_D because of lower effective voltage between the gate electrode and the membrane, whereas Q increases because of the lower voltage loading effect as we increase V_D.

We benchmark the displacement sensitivity of the resonators measured by direct i_D readout with the reported literature [Table I]. Utilizing strong quantum correlations in ultracoherent optomechanical systems, $S_x^{1/2} \approx \sim 0.01$ fm/Hz$^{1/2}$ has been demonstrated.[19] The exceptional sensitivity of single electron transistor (SET) at very low temperature enables motion detection by capacitively coupling it to the mechanical resonator and can achieve $S_x^{1/2} \approx \sim 2$ fm/Hz$^{1/2}$.[28] These demonstrations, however, require cryogenic cooling below 10 K and, thus, require bulky measurement system.[19,28] Optical interferometry can achieve $S_x^{1/2}$ as low as ~ 33.5 fm/Hz$^{1/2}$ while relying on laser.[19] The results presented in this work enable measuring $S_x^{1/2}$ as low as 0.5 pm/Hz$^{1/2}$, which does not require any cryogenic cooling or laser and better than capacitive readout reported in the literature.[29]

TABLE I. Benchmarking direct i_D readout in this work with other reported schemes.

Material/device	Dimension	Measurement technique/scheme	T	f_0 (MHz)	$S_i^{1/2}$ (A/Hz$^{1/2}$)	$S_x^{1/2}$ (m/Hz$^{1/2}$)	Ref
MoS_2 VCT	$d = 3$ μm, $h = 0.7$ nm	i_D measurement	293 K	31.83	7×10^{-12}	2.9×10^{-12}	This work
	$d = 3$ μm, $h = 1.4$ nm			21.43	2×10^{-12}	0.5×10^{-12}	
MoS_2 VCT	$l = 1.1$ μm, $w = 110$ nm	FM mixing	293 K	$\sim$111	N.A.	N.A.	10
Si_3N_4 beam with metallization	14 μm $\times$ 200 nm $\times$ 205 nm	Capacitive coupling	293 K	13.5	N.A.	4.1×10^{-12}	29
MoS_2 drumhead	$d = 5.5$ μm, $h = 38$ nm	Optical interferometry	293 K	14.13	N.A.	33.5×10^{-15}	2
Si cantilever	15.6 μm $\times$ 230 nm $\times$ 500 nm	Tapered fiber	293 K	1.13	N.A.	4×10^{-12}	30
Si_3N_4 string	3.6 mm $\times$ 3.6 mm $\times$ 20 nm	Optomechanical system	10 K	1.14	N.A.	1×10^{-17}	19
GaAs beam	3 μm $\times$ 250 nm $\times$ 200 nm	Single electron transistor	30 mK	116	N.A.	2×10^{-15}	28

Thus, direct i_D readout scheme holds promise for room temperature ultrasensitive displacement and force sensors that can be integrated with CMOS for on-chip applications.

In conclusion, we have demonstrated 1L- and 2L-MoS_2 VCTs and probed the resonance motion by directly measuring i_D. Both devices exhibit n-type transistor behavior with high I_{On} up to 0.1 μA/μm, I_{On}/I_{Off} exceeding 10^5, $\mu_E = 150\,cm^2/(V{\cdot}s)$, and near ideal SS = 98 mV/dec. We have utilized background subtraction to extract the current component due to resonance motion of the vibrating membrane. By fitting i_D after subtracting background, we have extracted resonances at $f_0 = 31.83$ MHz with $Q = 117$ and $f_0 = 21.43$ MHz with $Q = 110$ for 1L- and 2L-MoS_2 VCTs, respectively. The 2L-MoS_2 VCT demonstrates excellent pA current ($S_i^{1/2} = 2\,pA/Hz^{1/2}$) and pm displacement ($S_x^{1/2} = 0.5\,pm/Hz^{1/2}$) sensitivity. We have demonstrated f_0 tuning by controlling V_G and investigated the effect of V_D on f_0 and Q using 2L-MoS_2 VCT. The results suggest pathways to developing ultrasensitive on-chip displacement sensors at room temperature by exciting and probing the resonance motion all-electronically.

See the supplementary material for the fabrication process of MoS_2 NEMS resonators, Raman spectroscopy of 1 and 2L MoS_2 flakes, SEM imaging, discussions on resonance frequency calculation and simulation, and additional resonance characterization of 1L MoS_2 resonator.

We thank the financial support from the National Science Foundation (NSF) IUSE EHR Program (Grant No. DUE-2142552) and ECCS EAGER Program (Grant No. ECCS-2221881).

AUTHOR DECLARATIONS

Conflict of Interest

The authors have no conflicts to disclose.

Author Contributions

S M Enamul Hoque Yousuf: Conceptualization (equal); Data curation (lead); Formal analysis (lead); Investigation (equal); Methodology (equal); Validation (equal); Writing – original draft (lead); Writing – review & editing (equal). **Philip X. L. Feng:** Conceptualization (lead); Data curation (supporting); Formal analysis (equal); Funding acquisition (lead); Investigation (equal); Methodology (equal); Project administration (lead); Resources (lead); Supervision (lead); Writing – original draft (supporting); Writing – review & editing (equal).

DATA AVAILABILITY

The data that support the findings of this study are available from the corresponding author upon reasonable request.

REFERENCES

[1]A. K. Geim and K. S. Novoselov, Nat. Mater. **6**, 183–191 (2007).
[2]J. Lee, Z. Wang, K. He, J. Shan, and P. X.-L. Feng, ACS Nano **7**, 6086–6091 (2013).
[3]S M E. H. Yousuf, J. Lee, S. W. Shaw, and P. X.-L. Feng, J. Microelectromech. Syst. **32**, 335–346 (2023).
[4]B. Xu, P. Zhang, J. Zhu, Z. Liu, A. Eichler, X.-Q. Zheng, J. Lee, A. Dash, S. More, S. Wu, Y. Wang, H. Jia, A. Naik, A. Bachtold, R. Yang, P. X.-L. Feng, and Z. Wang, ACS Nano **16**, 15545–15585 (2022).
[5]J. Lee, Z. Wang, K. He, J. Shan, and P. X.-L. Feng, Sci. Adv. **4**, eaao6653 (2018).
[6]T. Mei, J. Lee, Y. Xu, and P. X.-L. Feng, Micromachines **9**, 312 (2018).
[7]F. Ye, A. Islam, T. Zhang, and P. X.-L. Feng, Nano Lett. **21**, 5508–5515 (2021).
[8]F. Wu, H. Tian, Y. Shen, Z. Hou, J. Ren, G. Gou, Y. Sun, Y. Yang, and T.-L. Ren, Nature **603**, 259–264 (2022).
[9]J. Lee, S. W. Shaw, and P. X.-L. Feng, Appl. Phys. Rev. **9**, 011404 (2022).
[10]S. Manzeli, D. Dumcenco, G. M. Marega, and A. Kis, Nat. Commun. **10**, 4831 (2019).
[11]Y. Yoon, K. Ganapathi, and S. Salahuddin, Nano Lett. **11**, 3768–3773 (2011).
[12]B. Radisavljevic, A. Radenovic, J. Brivio, V. Giacometti, and A. Kis, Nat. Nanotechnol. **6**, 147–150 (2011).
[13]K. F. Mak, C. Lee, J. Hone, J. Shan, and T. F. Heinz, Phys. Rev. Lett. **105**, 136805 (2010).
[14]H. K. Ng, D. Xiang, A. Suwardi, G. Hu, K. Yang, Y. Zhao, T. Liu, Z. Cao, H. Liu, S. Li, J. Cao, Q. Zhu, Z. Dong, C. K. I. Tan, D. Chi, C.-W. Qiu, K. Hippalgaonkar, G. Eda, M. Yang, and J. Wu, Nat. Electron. **5**, 489–496 (2022).
[15]X. Liu, A. Islam, and P. X.-L. Feng, in *Proceedings of the 20th International Conference on Solid-State Sensors, Actuators and Microsystems & Eurosensors XXXIII (TRANSDUCERS & EUROSENSORS XXXIII), Berlin, Germany, 23–27 June 2019* (IEEE, 2019), pp. 2408–2411.
[16]X.-Q. Zheng, T. Kaisar, and P. X.-L. Feng, Appl. Phys. Lett. **117**, 243504 (2020).
[17]K. Nishiguchi, H. Yamaguchi, and A. Fujiwara, Phys. Rev. Appl. **19**, L011003 (2023).
[18]J. Lee and P. X.-L. Feng, Appl. Phys. Lett. **119**, 243506 (2021).
[19]D. Mason, J. Chen, M. Rossi, Y. Tsaturyan, and A. Schliesser, Nat. Phys. **15**, 745–749 (2019).
[20]A. Islam, J. Lee, and P. X.-L. Feng, in *Proceedings of the IEEE International Conference on Micro Electro Mechanical Systems (MEMS)* (IEEE, 2018), pp. 1052–1055.
[21]R. Yang, Z. Wang, and P. X.-L. Feng, in *Proceedings of the IEEE International Conference on Micro Electro Mechanical Systems (MEMS)* (IEEE, 2016), pp. 59–62.
[22]V. Gouttenoire, T. Barois, S. Perisanu, J.-L. Leclercq, S. T. Purcell, P. Vincent, and A. Ayari, Small **6**, 1060–1065 (2010).
[23]A. Islam, J. Lee, and P. X.-L. Feng, in *Proceedings of the IEEE International Conference on Micro Electro Mechanical Systems (MEMS)* (IEEE, 2020), pp. 826–829.
[24]Y. Xu, C. Chen, V. V. Deshpande, F. A. DiRenno, A. Gondarenko, D. B. Heinz, S. Liu, P. Kim, and J. Hone, Appl. Phys. Lett. **97**, 243111 (2010).
[25]S. Bertolazzi, J. Brivio, and A. Kis, ACS Nano **5**, 9703–9709 (2011).
[26]Y. Du, L. Yang, J. Zhang, H. Liu, K. Majumdar, P. D. Kirsch, and P. D. Ye, IEEE Electron Device Lett. **35**, 599–601 (2014).
[27]C. Lee, H. Yan, L. E. Brus, T. F. Heinz, J. Hone, and S. Ryu, ACS Nano **4**, 2695–2700 (2010).
[28]P. A. Truitt, J. B. Hertzberg, C. C. Huang, K. L. Ekinci, and K. C. Schwab, Nano Lett. **7**, 120–126 (2007).
[29]O. Basarir, S. Bramhavar, and K. L. Ekinci, Nano Lett. **12**, 534–539 (2012).
[30]R. G. Knobel and A. N. Cleland, Nature **424**, 291–293 (2003).